

Magnetic Energy Storage and the Nightside Magnetosphere–Ionosphere Coupling

W. Horton, M. Pekker

Institute for Fusion Studies, The University of Texas, Austin, TX 78712

I. Doxas

Dept. of Astrophysical Planetary & Atmospheric Sciences, University of Colorado,

Boulder, CO 80309–0391

Short title: **MAGNETIC ENERGY STORAGE**

Abstract. The change in the magnetic energy stored in the Earth's magnetotail as a function of the solar wind IMF conditions are investigated using an empirical magnetic field model. The results are used to calculate the two normal modes contained in the low-dimensional global model called WINDMI for the solar wind driven magnetosphere-ionosphere system. The coupling of the magnetosphere-ionosphere (MI) through the nightside region 1 current loop transfers power to the ionosphere through two modes: a fast (period of minutes) oscillation and a slow (period of one hour) geotail cavity mode. The solar wind drives both modes in the substorm dynamics.

1. Introduction

In *Horton and Doxas* [1998] we presented a low-dimensional nonlinear dynamical model for the six major energy components of the solar wind driven magnetosphere–ionosphere. Here we call the model WINDMI and examine several aspects of the model in more detail.

The WINDMI model is derived by writing the electromagnetic field action $S_F(I, I_1, V, V_1)$ in terms of the two main current loops I, I_1 for the nightside magnetosphere and their associated voltages V, V_1 . The coupling of the electromagnetic fields to the plasma is through the interaction Lagrangian density $\mathcal{L}_I = \mathbf{j} \cdot \mathbf{A} - \rho\Phi$ where the current \mathbf{j} and charge ρ densities have both MHD and non-MHD contributions. In particular, the large gyroradius quasi-neutral sheet component of the geotail current \mathbf{j}_Σ determines the energy transfer to the mean central plasma sheet pressure $p_0(t)$ and the divergence of the parallel energy flux controls the unloading of the central plasma sheet pressure. The unloading events are defined by the critical geotail current I_c and the rate of unloading by the mean parallel flow velocity. By using the Lagrangian field formulation of the system, the model has a consistent mathematical structure giving a useful framework for a physics-based nonlinear prediction filter. In particular, in the absence of solar wind driving and ionosphere damping, the model conserves energy and is Hamiltonian. With solar wind driving and ionospheric damping, the model is consistent with Kirchhoff’s rules expressing the conservation of charge and energy. A block diagram of the components of the system, and the major feed-forward and feed-back loops is given in Fig. 1.

Solar Wind-Magnetosphere-Ionosphere WINDMI Backbone

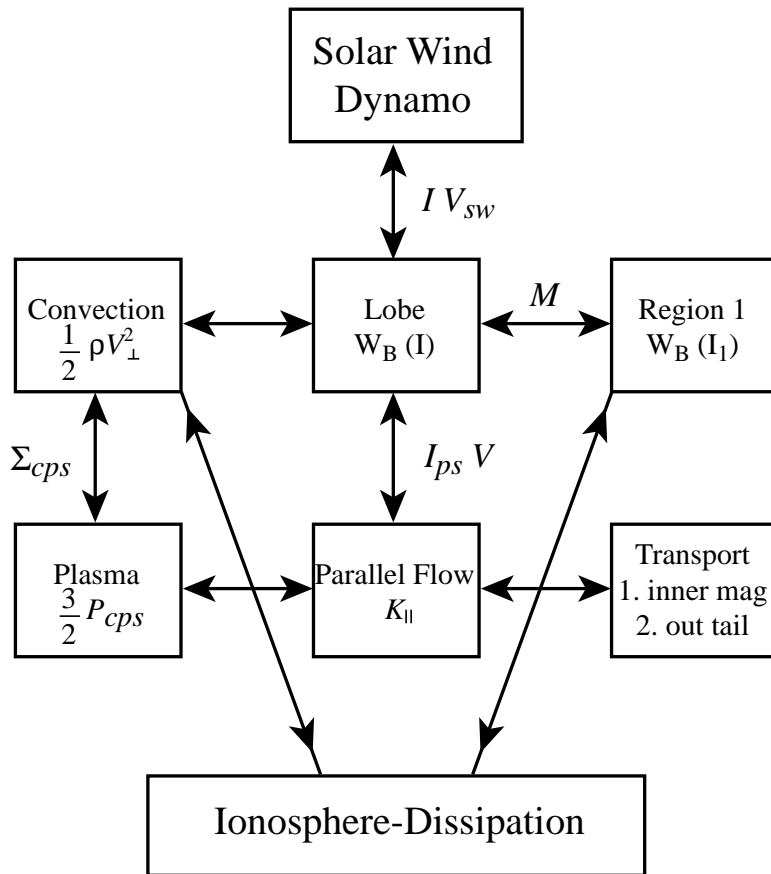


Figure 1. Interaction diagram for the six components of the solar wind driven magnetosphere-ionosphere.

The system has three fundamental time scales: (i) the global MHD cavity mode oscillations of geotail $\omega_0 \cong 1/(\mathcal{L}C)^{1/2} \cong 2\pi/1$ hr, (ii) the MI Alfvén coupling timescale $\omega_1 \cong 1/(\mathcal{L}_1 C_1)^{1/2} = 2\pi/10$ min, and (iii) the nonlinear RC_1 time of ionospheric damping. The electromagnetic coupling of the MI components in the WINDMI model, shown in Fig. 2, modifies these separate timescales in a way we will determine here. The electrodynamic coupling described by Fig. 2b controls the flow of the solar wind driven electrical power to the ionospheric load and the reaction of this load on the magnetotail system. The nonlinearity of the ionospheric decay time was shown to be a key ingredient

of the model in *Horton and Doxas* [1998]. The nonlinear ionospheric physics arises from the sharp increase of the ionospheric conductance with power deposited from the region 1 current loop. The detailed physics of the process for the precipitation of electrons into the ionosphere is regulated by the voltages V_1, V and the I_1 current.

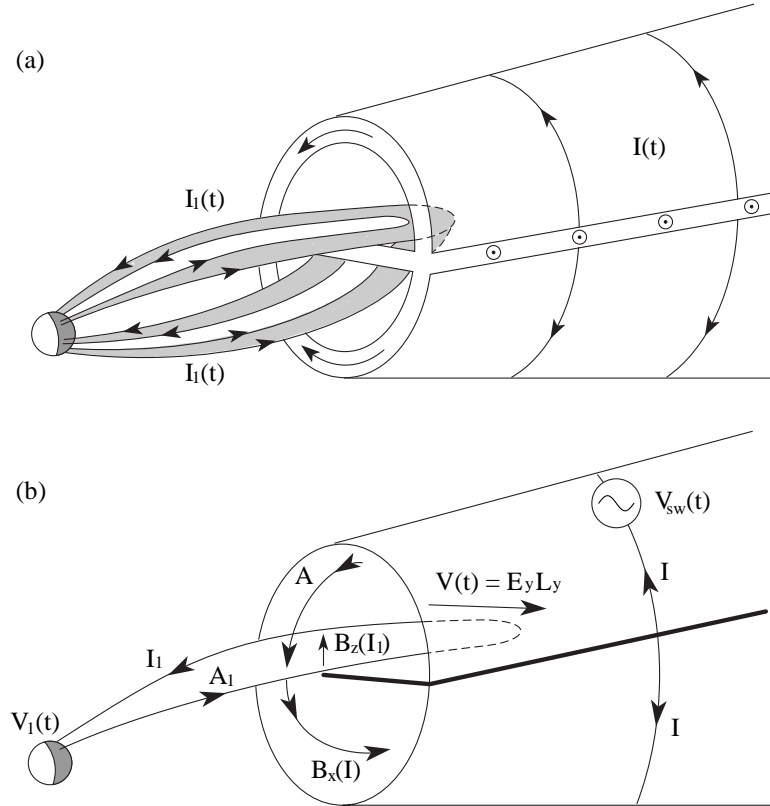


Figure 2. Diagrams that define the geometry of (a) the two current loops and (b) the mutual inductance and the voltages.

The southward turning of the IMF increases the magnetic stress which increases the energy stored in the nightside geomagnetic tail. The rate of this increase is given in Fig. 3 which shows the stored magnetic energy $W_B(\theta)$ as a function of the IMF clock angle θ . The computation of $W_B(\theta)$ is performed with the Tsyganenko-96 model that includes both the cross-tail current I and the region 1 current I_1 . The corresponding rate of change of the current $I(\theta)$ is shown in Fig. 3(b). The volume integrals include all the magnetospheric magnetic energy $B^2/2\mu_0$ beyond $x = -10 R_E$ due to the currents I and I_1 but excludes the B_{dp} from the Earth's dipole. The example in Fig. 3 is for the

case of a 10 nT IMF field magnetic that is rotated through the angle θ and for the solar wind dynamic pressure of 3 nPa. The $D_{st} = -150$ nT. These conditions correspond to the January 14/15, 1988 magnetic cloud event where the IMF rotates over a 30 hr period as given in *Farrugia et al.* [1993]. The first 12 hours after the initial pressure pulse has $B_z > 0$ and is substorm-free. As the IMF rotates, the first and largest substorm occurs with $\theta \simeq \pi/2$ ($B_y \simeq -20$ nT, $B_z \simeq 0$ nT) and then a sequence of substorms occurs for the 18 hr period with southward IMF.

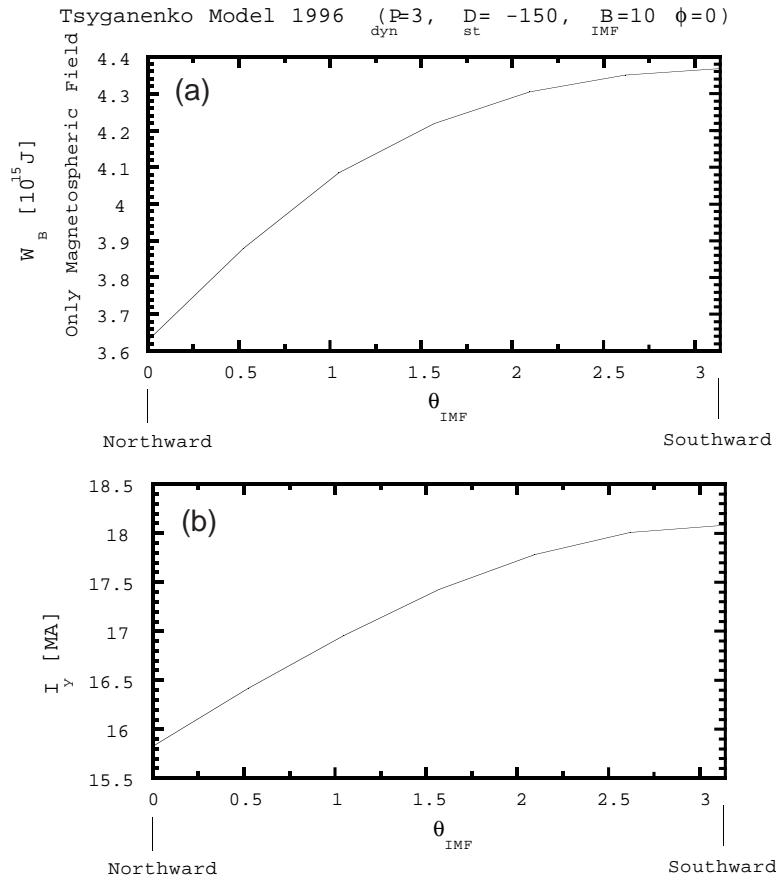


Figure 3. Increase of (a) the stored magnetic energy W_B and (b) the cross-tail magnetospheric current with rotation of the IMF magnetic field $B_0 = 10$ nT.

The rate of increase of the energy and current are most rapid for the initial IMF rotation away from pure northward toward the dawn-dusk direction. This strong initial increase of stored energy correlates with the *Farrugia et al.* [1993] magnetic cloud event

where the first substorm is a strong one occurring when the IMF has rotated to the dawn-dusk direction. Figure 3 indicates that at $\theta = \pi/2$ (the dawn-dusk direction) the stored energy has increased by approximately 16% from $3.6 W_0$ to $4.2 W_0$ in units of petajoules $W_0 = 10^{15}$ J. Completing the rotation from $\theta = \pi/2$ to $\theta = \pi$, the pure southward IMF gives the final stored energy a further 5% increase to 4.4×10^{15} J. The corresponding increase of the cross-tail current $I_y(\theta)$ in of Fig. 3(b) shows that the magnetic energy is well defined by $W_B = \frac{1}{2} \mathcal{L} I^2$, with the inductance $\mathcal{L} = 22$ to 24 H. In Fig. 4 we show 22 cycles of the system corresponding to the number of substorms in the 18 hr southward IMF.

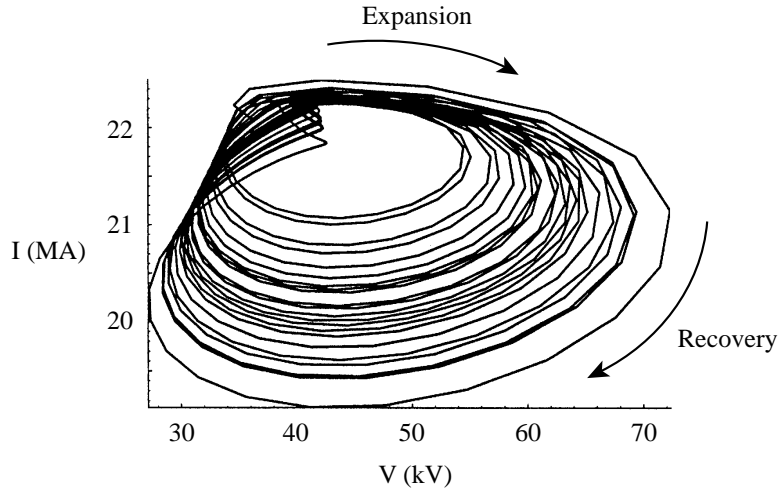


Figure 4. Projection on the I, V plane of the irregular periodic system trajectories during the constant applied $v_x B_s$ driver from the solar wind.

In the Farrugia data during the southward IMF there is an irregular sequence of 22 substorms with mean recurrence time of approximately 50 min. Both the *Horton and Doxas* [1996] model and the *Klimas et al.* [1994] model show the weakly chaotic pulsations in the constant southward IMF period. Under these conditions the magnetosphere has a chaotic attractor with the irregular limit cycle shown in the figure. The average period is about 50 min depending on the exact values of the inductance, capacitance and the unloading trigger. The onset condition for the pulsations in the model is controlled by the Hopf bifurcation conditions for the system. The bifurcation

analysis [*Horton and Doxas, 1996*] is complicated but explains the details of the cycling of the system between loading and the unloading of substorms.

During the growth phase of the cycle the geotail current is increasing in time (left portion of the cycles shown in Fig. 4) which induces a positive EMF in the nightside region 1 current loop increasing the westward electrojet current. A growth of the geotail current by 1 MA per minute induces approximately 100 kV in the region 1 current loop. The growth of the nightside region 1 current I_1 reduces the net current $I - I_1$ in the closure region of the geotail. This reduction of the net geotail current appears as a current diversion. After the onset of the unloading there is a large, rapid increase of the dawn-dusk electric field in both the geotail and in the ionosphere. In the example shown the maximum geotail field exceeds the constant driving voltage by 50%. During this period there is a large increase in both the $\mathbf{E} \times \mathbf{B}$ and parallel flow velocities. The system then enters the recovery phase where both the current and the voltage are decreasing. Here the plasma pressure begins to increase again as the parallel kinetic energy has dropped to a low level.

The currents are distributed over large regions that are not precisely known. Both MHD simulations [*Brecht et al., 1982; Steinolfson and Winglee, 1993; Fedder and Lyon, 1995; Birn and Hess, 1996*] and empirical magnetic field models, such as *Tsyganenko, [1989, 1996]*, give useful information about the distribution of the currents. The empirical satellite-based magnetospheric models yield the magnetic field energy $W_B(I, I_1)$ produced by the geotail current I and the nightside region 1 current loop I_1 . The expansion of W_B in terms of the currents yields the inductances. For a distributed current system the values of the self and mutual inductances of the dominant current loops are defined by the decomposition

$$W_B = \frac{1}{2} \mathcal{L} I^2 - M I I_1 + \frac{1}{2} \mathcal{L}_1 I_1^2 \quad (1)$$

where explicit (Jackson, p. 261) volume integrals over the current densities $\mathbf{j}(\mathbf{x})$ can be

written for \mathcal{L} , M , \mathcal{L}_1 . In addition to the plasma associated magnetic energy $W_B(I, I_1)$ there is the Earth's dipole magnetic energy $W_{dp} \simeq 770 \times 10^{15}$ J. The dipole energy beyond a radius R is $W_{dp}(R_E/R)^3$ and is thus negligible ($\lesssim 0.77 W_0$) compared to W_B for $R > 10 R_E$. Likewise the ring current contribution is small beyond $10 R_E$. Thus, we have evaluated the self-inductance and the mutual inductances directly from the variation of the geotail magnetic energy variation with I and I_1 from the Tsyganenko-96 model.

The determination of \mathcal{L}_1 and M evolves more uncertainty since the energy components are smaller and the geometry of the nightside region 1 current is more complex. Our analysis based on both the Tsyganenko-96 model and the performance of the WINDMI model on the Bargatze database lead to $\mathcal{L}_1 = 10$ H and $M = 5$ H to 10 H. The value of M may be as large as 10 H without affecting the performance of either model. Smaller values of \mathcal{L}_1 and M can be ruled out by arguments based on the geometry of nightside magnetosphere. From Fig. 2 it is clear that growth of the magnetotail current $I(t)$ produces a negative ΔB_z in the Earthward edge of the central plasma current sheet that links the I_1 -current loop with $M = \mu_0 L_{yI} \ell n(L_{xI}/D) \sim 10$ H where L_{xI} is the length of the region 1 and L_{yI} is the dawn-dusk dimension of the region 1 current loop in the central plasma sheet.

The geotail and nightside region 1 current systems, however, are intrinsically coupled. Thus we find the transformation to the two normal mode frequencies and eigenvectors of the MI system. The procedure is to first neglect the ionospheric damping to find the normal modes of the underlying 2-degree-of-freedom Hamiltonian.

The definitions for the capacitances follow from reducing the electric field energy

$$W_E = \frac{1}{2} \int \epsilon_{\perp}(x) E_{\perp}^2 d^3x = \frac{1}{2} C_{\text{cps}} V^2 + \frac{1}{2} C_1 V_1^2 \quad (2)$$

where $\epsilon_{\perp} = \rho_m(\mathbf{x})/B^2(\mathbf{x})$ accounts for the polarization of the plasma. Thus, the electric field energy is the kinetic energy from plasma convection $W_E = \frac{1}{2} \int \rho_m v_E^2 d^3x$ where

$$\mathbf{v}_E = \mathbf{E} \times \mathbf{B}/B^2.$$

With no forcing and damping we write the Lagrangian in terms of the generalized coordinates q_1, q_2 where

$$L(q, \dot{q}) = \frac{1}{2} \dot{q}_i T_{ij} \dot{q}_j - \frac{1}{2} q_i V_{ij} q_j \quad (3)$$

with $\dot{q}_1 = I - I_1$ and $\dot{q}_2 = I_1$. The q 's may be interpreted as the effective charges associated with the capacitances C and C_1 . The 2×2 symmetric matrices \mathbf{T} and \mathbf{V} have elements $T_{11} = \mathcal{L}, T_{12} = T_{21} = \mathcal{L} - M, T_{22} = \mathcal{L} + \mathcal{L}_1 - 2M$ and $V_{11} = 1/C, V_{22} = 1/C_1, \text{ and } V_{12} = 0$. The normal modes are found from the eigenvalue problem $\omega_\ell^2 \mathbf{T} \cdot \mathbf{a}_\ell = \mathbf{V} \cdot \mathbf{a}_\ell$. Forming the 2×2 matrix \mathbf{A} with columns \mathbf{a}_1 and \mathbf{a}_2 gives the transformation $\mathbf{q}(t) = \mathbf{A} \cdot \boldsymbol{\zeta}(t)$ to the normal modes $\boldsymbol{\zeta}(t)$. The transformation is canonical with old momenta $\boldsymbol{\pi}_i = \partial L / \partial \dot{\mathbf{q}}_i = \mathbf{T} \cdot \dot{\mathbf{q}}$. Transformed to the uncoupled form of the normal modes $\zeta_1(\ell = 1)$ and $\zeta_2(h = 2)$ the Hamiltonian is

$$H(p_\zeta, \zeta) = \frac{1}{2} \dot{\zeta}_\ell^2 + \frac{1}{2} \omega_\ell^2 \zeta_\ell^2 + \frac{1}{2} \dot{\zeta}_h^2 + \frac{1}{2} \omega_h^2 \zeta_h^2 \quad (4)$$

where ω_ℓ and ω_h are the lowest and the highest eigenfrequencies of the coupled system. The transformation matrix \mathbf{A} has the properties $\mathbf{A}^T \mathbf{T} \mathbf{A} = \mathbf{I}$ and $\mathbf{A}^T \mathbf{V} \mathbf{A} = \boldsymbol{\lambda}$ where \mathbf{A}^T is the transpose of \mathbf{A} . We will not write the somewhat lengthy formulas in detail, but instead give the values $\omega_\ell = 1.53 \times 10^{-3}$, $\omega_h = 1.19 \times 10^{-2}$ and the eigenvectors $\mathbf{x}_\ell = (.996, .085), \mathbf{x}_h = (-.608, .795)$ for the two normal modes. For the low frequency mode $I_1/I \simeq 0.085$ and for the high frequency mode $I_1/I \approx 4$. These values are for $\mathcal{L} = 40 \text{ H}, \mathcal{L}_1 = 10 \text{ H}, M = 10 \text{ H}, C = 10^4 \text{ F}$ and $C_1 = 10^3 \text{ F}$.

Thus, in this example the low-frequency geotail cavity mode has a period of 1.1 hr with ΔI_1 about 10% of ΔI . The high frequency mode has a period of 8.8 min with ΔI about 25% of ΔI_1 . Both modes are large scale Alfvén modes as one can show from the analytic formulas for \mathcal{L} and C . The full WINDMI system shown in Fig. 1 is a complex dynamical system with additional timescales. The normal modes in Eq. (4) are in some sense the underlying backbone of the complex system.

For a weak coupling approximation we find that the low frequency mode is given approximately by $\omega_\ell \simeq [\mathcal{L}(C + C_1)]^{-1/2}$ and $\omega_h = [\mathcal{L}_1(1 - \bar{m}^2)]^{-1/2} [\frac{1}{C} + \frac{1}{C_1}]^{1/2}$ where $\bar{m} = M/(\mathcal{L}\mathcal{L}_1)^{1/2}$. In the numerical example above $\bar{m} = 1/2$. Thus, in the low frequency oscillations $V \simeq V_1$ as in *Boyle and Reiff* [1997] and the capacitances act in parallel. For the high frequency oscillations the capacitances act in series and $M dI/dt$ drives the I_1, V_1 current loop.

2. Conclusions

The WINDMI model has six energy components thought to be essential in describing the state disturbed times of the magnetotail-ionospheric system. These components are also the key energy components of the resistive MHD dynamics of reconnection. They are: (1) lobe magnetic field energy: $\int_{\text{lobe}} \frac{B^2}{2\mu_0} d^3x = \frac{1}{2} \mathcal{L}I^2$ ($\sim 4 \times 10^{15}$ J); (2) $\mathbf{E} \times \mathbf{B}$ kinetic energy: $\int_{\text{cps}} \frac{1}{2} \rho_m u_\perp^2 d^3x = \frac{1}{2} C_{\text{cps}} V^2$ ($\sim 4 \times 10^{13}$ J); (3) parallel kinetic energy: $\int_{\text{cps+psbl}} \frac{1}{2} \rho_m u_\parallel^2 d^3x = K_\parallel$ ($\sim 3 \times 10^{14}$ J); (4) central plasma sheet thermal energy: $U_p = \int_{\text{cps}} (P_\perp + \frac{1}{2} P_\parallel) d^3x \cong \frac{3}{2} P \Omega_{\text{cps}}$ ($\sim 3 \times 10^{14}$ J); (5) ionospheric $\mathbf{E} \times \mathbf{B}$ kinetic energy: $W_i = \frac{1}{2} C_1 V_1^2$ ($\sim 3 \times 10^{12}$ J); and (6) ionospheric magnetic energy: $\frac{1}{2} \mathcal{L}_1 I_1^2$ ($\sim 10^{12}$ J) associated with the region 1 current.

Here we analyze the strength of the interaction of the two current loops I, I_1 through the interaction component $W_{gt,i} = -MII_1$ from the magnetic flux linkage of the lobe magnetic field from I through the region 1 current loop as indicated by Fig. 2. Knowledge of the interaction between the two plasma current loops is important to understanding the power transfer to the ionosphere from the solar wind dynamo.

The WINDMI model gives a mathematical self-consistent backbone for describing the complex system dynamics of the solar wind driven magnetosphere-ionospheric systems.

Acknowledgments. The work was supported by the NSF Grant No. ATM-97262716 and NASA Grant NAGW-5193.

References

- Bargatze, L.F., D.N. Baker, R.L. McPherron, and E.W. Hones, Magnetospheric impulse response for many levels of geomagnetic activity, *J. Geophys. Res.* **90**, 6387–6394 (1985).
- Birn, J., and M. Hesse, Details of current disruption and diversion in simulations of magnetotail dynamics, *J. Geophys. Res.* **101**, 15,345–15,358 (1996).
- Boyle, C.B., and P.H. Reiff, Empirical polar cap potentials, *J. Geophys. Res.* **102**, 111–125 (1997).
- Brecht, S.H., J.G. Lyon, J.A. Fedder, and K. Hain, A time dependent three-dimensional simulation of the Earth's magnetosphere: Reconnection events, *J. Geophys. Res.* **87**, 6098 (1982).
- Farrugia, C.J., M.P. Freeman, L.F. Burlaga, R.P. Lepping, and K. Takahashi, The Earth's magnetosphere under continued forcing: Substorm activity during the passage of an interplanetary magnetic cloud, *J. Geophys. Res.* **98**, 7657 (1993).
- Fedder, J.A., and J.G. Lyon, The Earth's magnetosphere is $165 R_E$ long: Self-consistent currents, convection, magnetospheric structure, and processes for northward interplanetary magnetic field, *J. Geophys. Res.* **100**, 3623–3635 (1995).
- Horton, W., and I. Doxas, A low-dimensional energy conserving state space model for substorm dynamics, *J. Geophys. Res.* **101A**, 27,223–27,237 (1996).
- Horton, W., and I. Doxas, A low-dimensional dynamical model for the solar wind driven geotail-ionosphere system, *J. Geophys. Res.* **103A**, 4561 (1998).
- Jackson, John David, *Classical Electrodynamics*, (2nd Ed.), (John Wiley & Sons, New York, 1975).
- Klimas, A.J., D.N. Baker, D. Vassiliadis, and D.A. Roberts, Substorm recurrence during steady and variable solar wind driving: Evidence for a normal mode in the unloading dynamics of the magnetosphere," *J. Geophys. Res.* **99**, 14,855 (1994).

Steinolfson, R.S., and R.M. Winglee, Energy storage and dissipation in the magnetotail during substorms. 2. MHD simulations, *J. Geophys. Res.* **98**, 7537 (1993).

Tsyganenko, N.A., A magnetospheric magnetic field model with a warped tail current sheet, *Planet Space Sci.* **37**, 5 (1989).

Tsyganenko, N.A., and D.P. Stern, Modeling of the global magnetic field of the large-scale Birkeland current systems, *J. Geophys. Res.* **101**, 27187–27198 (1996).

W. Horton and M. Pekker, Institute for Fusion Studies, The University of Texas, Austin, TX 78712 (e-mail: horton@peaches.ph.utexas.edu)

I. Doxas, Department of Astrophysical Planetary and Atmospheric Sciences, University of Colorado, Boulder, CO 80309–0391 (e-mail: doxas@callisto.colorado.edu)

Received _____